The Influence of Topography and Ambient Stability on the Characteristics of Cold-Air Pools: A Numerical Investigation

MARWAN KATURJI AND SHIYUAN ZHONG

Department of Geography, Michigan State University, East Lansing, Michigan

(Manuscript received 15 August 2011, in final form 23 April 2012)

ABSTRACT

A high-resolution numerical investigation of a cold-air pooling process (under quiescent conditions) is carried out that systematically highlights the relations between the characteristics of the cold-air pools (e.g., slope winds, vertical temperature and wind structure, and cooling rate) and the characteristics of the topography (e.g., basin size and slope angle) under different ambient stabilities. The Advanced Regional Prediction System model is used to simulate 40 different scenarios at 100-m (10 m) horizontal (vertical) resolution. Results are within the range of similar observed phenomena. The main physical process governing the cooling process near the basin floor (<200 m in height) was found to be longwave radiative flux divergence, whereas vertical advection of temperature dominated the cooling process for the upper-basin areas. The maximum downslope wind speed is linearly correlated with both basin size and slope angle, with stronger wind corresponding to larger basin and lower slope angle. As the basin size increases, the influence of slope angle on maximum downslope wind decreases and the maximum is located farther down the slope. These relationships do not appear to be sensitive to stability, but weaker stability produces more cooling in the basin atmosphere by allowing stronger rising motion and adiabatic cooling. Insight gained from this study helps to improve the understanding of the cold-air pooling process within the investigated settings.

1. Introduction

Cold-air pools (CAPs) are cold air that resides in terrain pockets surrounded by elevated topography. A CAP has weak and variable winds, is colder than overlying air, has a stable core-temperature profile, and is capped along ridge heights by a temperature inversion with varying intensity and depth (Whiteman et al. 2001). If a CAP resists a diurnal warming or synoptic displacement it can persist for up to 2 weeks, thus becoming a ''persistent CAP.'' Persistent CAPs suppress vertical mixing, increase ground-level air pollution, and decrease visibility to hazardous conditions in urbanized valleys and basins (Smith et al. 2010; Malek et al. 2006). Current research on CAPs has been conducted for inhabited valleys that vary from a few hundred square meters in areal coverage (Whiteman et al. 1999) to tens of square kilometers (Whiteman et al. 2001; Zhong et al. 2001; Rakovec et al. 2002) as well as for some enclosed basins or sinkholes (Clements et al. 2003; Whiteman et al. 2004; Steinacker et al. 2007). Climatological analyses of persistent CAPs in the western United States (Wolyn and McKee 1989; Reeves and Stensrud 2009) revealed that they are mainly wintertime events that are initiated either by cold-air frontal advection into terrain pockets or by a typical nighttime temperature inversion under clear skies, which is enhanced as warm air aloft advects, descending and deepening the stable layer. The persistent CAP is then efficiently destroyed when strong disturbances associated with a regional trough move over the area. The onset and maintenance of persistence CAPs have been verified by smaller observational datasets and modeling analyses (Lee et al. 1989; Whiteman et al. 1999, 2001; Zhong et al. 2001; Zängl 2005; Hoggarth et al. 2006).

Understanding the characteristics of CAPs can aid in a better understanding of this phenomenon and can possibly improve its prediction. Most of the current modeling studies address questions that target specific observational case studies, and this research has provided the current knowledge and understanding of CAP dynamics. In this study, we used a systematic numerical modeling approach to investigate the characteristics of CAPs (e.g., vertical temperature structure and cooling

Corresponding author address: Marwan Katurji, Dept. of Geography, Michigan State University, East Lansing, MI 48824.
E-mail: katurji@msu.edu

DOI: 10.1175/JAMC-D-11-0169.1

rates of the basin and slope environments) and their relationships to ambient stability, basin size, and slope angles. The goal is to build a framework upon which the results of high-resolution numerical modeling of the cooling process of a basin environment are assessed and are compared with relevant observations and other modeling results.

2. Method

a. Model and simulation setup

For simulating a CAP under quiescent nighttime conditions in a basin environment we have chosen the Advanced Regional Prediction System (ARPS; Xue et al. 2000, 2001). ARPS is a nonhydrostatic compressible atmospheric model that is designed to perform simulations on regional scales to the microscale with a terrain-following coordinate system. ARPS has been validated in numerous studies (e.g., Chow et al. 2006; Weigel et al. 2006) and also has been cross compared with other models for different atmospheric stability conditions (Fedorovich et al. 2004; Beare et al. 2006). For this study, the ARPS simulations are strictly two dimensional (2D) with an adequate number of grid points (varying between 299 and 1043) in the west–east direction to minimize numerical contamination at the inflow boundary for different topographical scenarios. The setup has four grid points in the crosswind direction (north–south), with one central grid point on which the solution is carried out and one and one-half grid points on each side for boundary conditions (scalar and vector quantities). A wave-radiation open boundary condition (Klemp and Durran 1983) was used at the inflow boundary, and periodic conditions were applied at crosswind boundaries (north–south), which allows for an infinitely long north–south direction with no flow simulation from that direction. Coriolis force was neglected because of the 2D idealized settings and the relatively small spatial (maximum basin width of 16 km) and temporal (8 h) scales. The subgrid-scale turbulence local closure scheme used was the 1.5-order turbulent kinetic energy model. The horizontal grid spacing was 100 m, and the vertical grid is stretched following a hyperbolic tangent equation with minimum grid spacing of 10 m near the surface, increasing to 20 m at midbasin height (500 m) and to a maximum of 190 m at model top (10 km). The simulations assumed clear-sky conditions, and therefore no microphysics or cloud processes were included. The radiative schemes adopted in ARPS were after Chou (1990, 1992) and Chou and Suarez (1994) and include a full radiative transport mechanism. For further descriptions of ARPS model physics see Xue et al. (2000, 2001), and for an alternative example and performance of a 2D-ARPS model setup refer to Katurji et al. (2011).

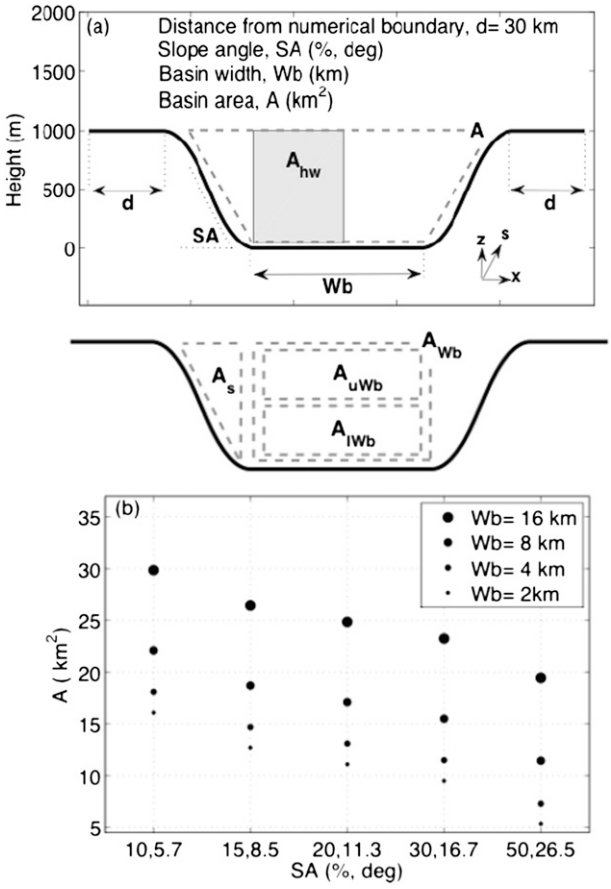

FIG. 1. A schematic of topography shape and dimensions used in the simulations. (a) Various basin areas within which the analysis was performed. (b) The calculated basin area A, representing the cross-sectional area of the enclosed air within the basin, as a function of slope angle SA and basin width Wb.

b. Experimental design

The topography was chosen to represent a simplified basin (1000 m deep), slope, and plateau setting as shown in Fig. 1a along with the basin widths Wb, slope angles SA, and basin cross-sectional areas A for the 20 different simulations (Fig. 1b) for each of the two atmospheric ambient stabilities chosen (a total of 40 simulations). The width of the basin decreases from 16 km, which scales to a medium-size populated basin such as Utah's Salt Lake basin, to 2 km, which represents small basins/sinkholes such as Colorado's Sinbad basin. The slope angles approximate real slope values, starting at 5.7° and reaching a steep slope of 26.5°. The initial and ambient atmospheric temperature profiles were determined on the basis of derived mean vertical profiles of temperature from climatological and experimental studies of persistent CAPs (Wolyn and McKee 1989; Reeves and Stensrud 2009; Whiteman et al. 2001).

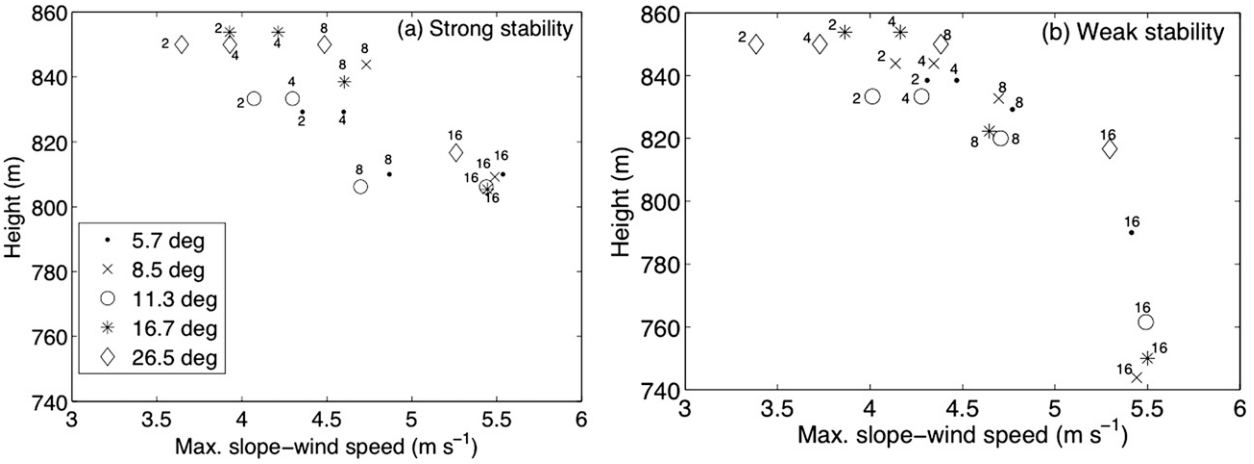

FIG. 2. The height (measured from basin floor) of maximum downslope wind speed as a function of slope angle and basin width at hour 8 of the simulation for the (a) strong-stability and (b) weak-stability cases. Symbols denote different slope angles, and the number labels represent different basin widths.

Two atmospheric stability conditions were considered: the strong-stability case with a temperature inversion of +6 K km^{-1} and the weak-stability case with near-isothermal (+0.2 K km^{-1}) conditions. Initial wind speeds for all 40 simulations were set to zero, and the simulations were run for an 8-h nighttime period in a midlatitude region.

3. Results

The analyses of the results are based on examination of cooling trends and evolved flow structure as a function of basin shape (in terms of its size and slope angle) and the background atmospheric stability. The basin and slope surfaces cool as a result of surface net-radiative energy loss, which leads to a negative sensible heat flux that cools adjacent air layers and results in downslope flow and convergence on the basin floor (Yoshino 1984). This process creates rising motion in the basin center and further cools the upper-air layers by adiabatic expansion. This process continues until the basin floor is covered by a strong surface-based inversion and cools considerably to allow for relatively warmer (less dense) downslope flow detrainment from the slope into and over the more stable air within the surface inversion (Baines 2001; Princevac et al. 2005). The flow that separates from the slope can also converge over the surface-based inversion and rise, further cooling the upper-basin layers.

a. Downslope wind

We first examine the magnitude of the maximum downslope wind speed and the location of its occurrence up the slope and relate these properties to the basin area and slope angle. The maximum downslope winds were attained by inspecting the grid points over the slope at all vertical and horizontal levels, and they almost always occurred at the first model vertical level above the slope surface; a higher vertical resolution would have been required to resolve a near-surface downslope jet. The maximum wind speed (5.5 m s^{-1}) was attained for the largest basin having the weakest slope gradient, whereas the minimum wind speed (3.5 m s^{-1}) occurred for the smallest basin having the strongest slope gradient. These simulated downslope wind speeds fall within observed values of nocturnal slope flows for different slope angles (Whiteman and Zhong 2008; Zhong and Whiteman 2008; Haiden and Whiteman 2005; Monti et al. 2002).

The location of the downslope wind speed maxima up the slope, as defined by height above basin floor, and its relation to the slope angle and basin size are shown in Fig. 2. As the basin gets smaller the maximum downslope wind speed magnitude is reduced and is located farther up the slope, whereas for the larger basins (Wb = 16 km) the rate of cooling of the basin atmosphere is less (as discussed in the following section), especially for the upper area of the basin (Fig. 2a) and as a consequence the cold air flowing down the slope attains its quasi-neutral buoyancy farther down the slope.

The relationship between the maximum downslope wind speed and the basin area and slope angle is shown in Fig. 3. In general, the downslope wind speed appears to be very well correlated with the basin size (dotted line) and the slope angle (solid lines), with stronger wind corresponding to larger basin and lower slope angle. These results may be explained by an examination of momentum budget equation for the along-slope

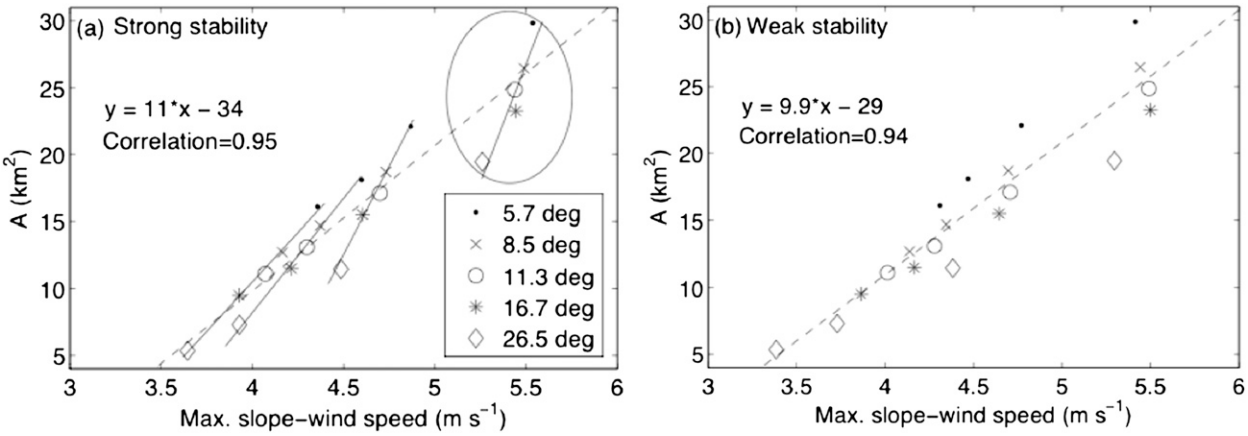

FIG. 3. Maximum downslope wind speeds at hour 8 of the simulation as a function of A and SA for the (a) strong-stability and (b) weak-stability cases. The dashed line is the best fitting to all data points with the linear equation and correlation coefficient shown in the panel.

wind component, neglecting the Coriolis force (Mahrt 1982):

$$\frac{\partial u_s}{\partial t} = -\frac{1}{\rho}\frac{\partial p}{\partial x}\cos\alpha + g\frac{\theta_2 - \theta_1}{\theta_1}\sin\alpha - \frac{\partial \overline{u_s' w_n'}}{\partial n}, \quad (1)$$

(I) (II) (III) (IV)

where u_s and w_n are the along-slope and normal wind components, ρ is air density, p is the air pressure, g is the gravitational acceleration, θ is air potential temperature, x is the Cartesian coordinate (Fig. 1a), s is the along-slope coordinate (positive up the slope), n is the normal-slope component, t is time, and α is the slope angle. Terms I–IV represent the downslope wind speed tendency, along-slope component of the horizontal pressure gradient force, buoyancy force, and turbulent dissipation, respectively. Points 1 and 2 represent the locations on the slope surface and the corresponding same-height location above the basin center, respectively. As shown by the dotted line in Fig. 3, which is the best fit to all data points, the maximum downslope wind speed increases linearly as the basin area increases. This is because the larger basins correspond to stronger horizontal wind speeds within the basin environment (Figs. 4e,f), suggesting that the pressure gradient force directed from the slope to the center of the basin is higher. Thus term II of Eq. (1) increases as the basin area increases. If we were to use the bulk average temperature difference between the slope environment (averaged for area A_s in Fig. 1a) and the same height above the basin floor (averaged for area A_{uWb}) to represent the temperature differences in term II, we would also find out that the difference of this temperature gradient between the large and small basin areas also increases (taking temperatures at hour 8 in Fig. 7, discussed in detail below). Hence, terms II and III increase together as the basin area increases, yielding a higher downslope wind speed for wider basins.

A closer examination of Fig. 3 reveals that, although the linear relationship between maximum downslope wind speed and the basin size exists for all slope angles, the rate of change is slightly affected by the slope angles. For example, the rate of increase of maximum downslope wind speed with basin size along a line passing through the diamonds representing a 26.5° steep slope is faster than that along a line through the dots representing a 5.7° gentle slope. In other words, a steeper sidewall slope corresponds to a higher rate at which maximum downslope wind speed increases with the area of the basin.

For the case of varying slope angles the relationship between the maximum downslope wind speed and the slope angle remains linear (solid linear trend lines in Fig. 3), but the maximum downslope wind speed becomes less sensitive to the slope angle for larger basin areas (as shown by the increase of slope of the solid linear trend line as the basin area increases). To explain this by referring to Eq. (1), a decrease in slope angle α would lead to an increase in term II and a decrease in term III; also, as α decreases, the basin area increases (as shown in Fig. 1), resulting in a further increase of term II, as discussed in the paragraph above. Hence, a lower slope angle corresponds to an increase in downslope wind speed tendency [Eq. (1)] and therefore higher maximum downslope wind speed. As the basin area gets larger, the effect of the slope angle on terms II and III diminishes and the relationship between the maximum downslope wind and slope angle becomes weaker (as shown by the decreased tilt of trend line for larger areas in Fig. 3a).

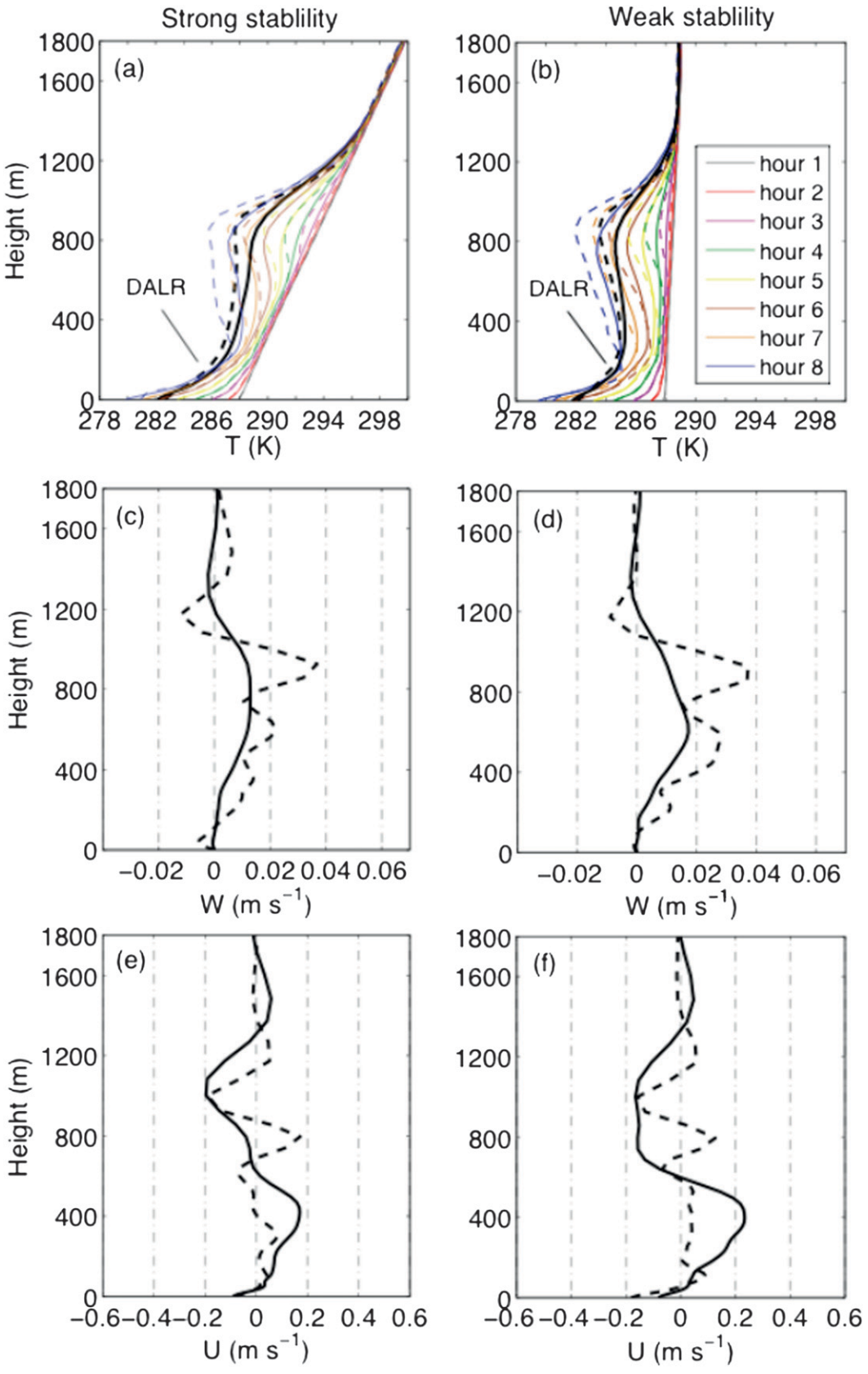
Strong stablility
Weak stablility
(a)
(b)
(c)
(d)
(e)
(f)
Height (m)
T (K)
W (m s^{-1})
U (m s^{-1})
DALR
hour 1
hour 2
hour 3
hour 4
hour 5
hour 6
hour 7
hour 8

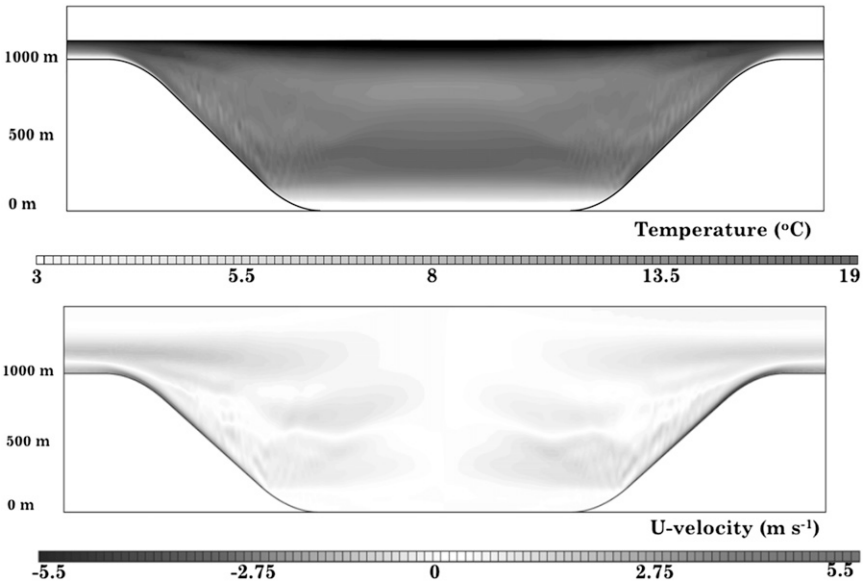

FIG. 5. Time–height cross section of temperature and u velocity (positive sign for flow from left to right) for the 16-km-wide basin (5.7° slope angle) at hour 8 of the strong-stability-case simulation.

b. Vertical structure and evolution

Figure 4 shows the basin half-width area-averaged (A_{hw} in Fig. 1a) vertical profiles of temperature T and horizontal U and vertical W wind components for the largest and the smallest basin and for the two stability cases. We have chosen the basin half-width area average to reduce the unnecessary postprocessing computational cost because the flow fields are horizontally homogeneous and are nearly symmetric about the center (Fig. 5). The cross-sectional area of the small basin was one-sixth of the area of the largest basin, with widths and slope angles as shown in Fig. 1b. The large and small basins show very similar cooling rates for the first 200 m above the basin floor (Figs. 4a,b). The near-surface air cooled 8 K in 8 h (cooling rate of 1 K h^{-1}), with a strong temperature inversion of approximately 10 K from the surface to ~200 m at hour 8 for the large and small basins and the strong- and weak-stability cases, and with weak U velocities (Figs. 4e,f). Inversions of this strength are not uncommon and have been previously observed in canyons and valleys (Whiteman et al. 1999). The 8-h averaged profiles in Figs. 4a,b, also reveal similar temperature gradients near the surface, but in the strong-stability case (Fig. 4a) the upper-level air between 200 and 1000 m cools more for the smaller basin, and this is explained by the relatively higher W velocity for the smaller basin than for the large basin in the same height range (Fig. 4c), which results in more adiabatic expansion associated with air lifting. The weak-stability case (Figs. 4b,d) shows similar behavior, but the resulting temperature profile between 200 and 1000 m is less stable. Although the magnitudes of vertical motion are very weak, adiabatic cooling associated with the weak rising motions is enough to cool the upper-basin layers by 1 K. A capping temperature inversion is formed over the top of the basin as a result of the subsidence (negative W velocity; Figs. 4c,d) associated with the return flow (negative U velocity; Figs. 4e,f) at the height levels above the basin rim (900–1200 m). This capping inversion is stronger for the smaller basin

←

FIG. 4. Vertical profiles of spatially averaged (over basin half-width area A_{hw}; see Fig. 1a) (a),(b) temperature and (c),(d) vertical and (e),(f) horizontal velocity (positive u velocity sign is for flow from left to right and vice versa for negative u velocity sign) for (left) the strong- and (right) weak-ambient-stability cases. The largest and smallest basins are shown by the solid and dashed lines, respectively. The 8-h averages are shown in black; 1-hourly temperature profiles in (a) and (b) are shown in colors. DALR corresponds to the dry-adiabatic lapse rate. The large and small basins correspond to the upper-left and lower-right points in Fig. 1b.

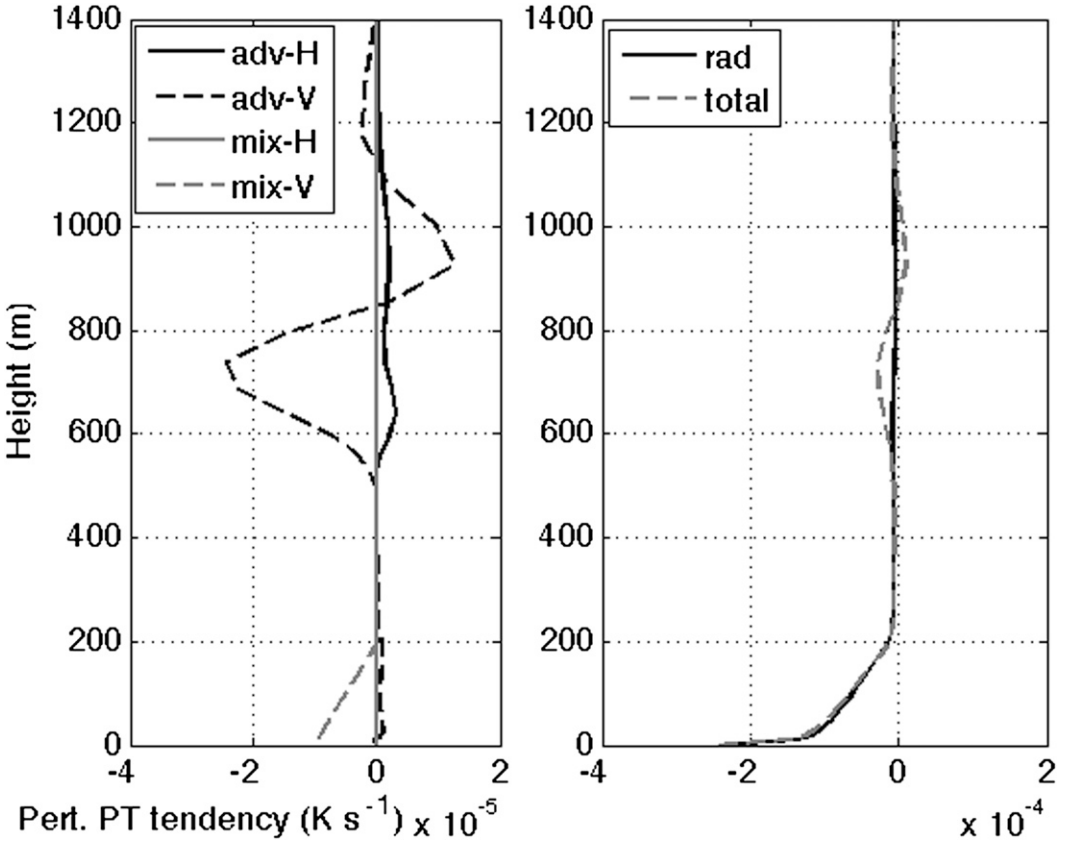

FIG. 6. (left) Vertical profile of spatially (over A_{hw}; see Fig. 1a) and time-averaged (8-h) perturbation potential temperature tendency terms for the 16-km-wide basin (5.7° slope angle). Advection (mixing) terms are shown in black (gray) lines, and horizontal (vertical) terms are shown in solid (dashed) lines. (right) Radiation and total tendency.

mainly because of the stronger subsidence as depicted by the W velocity (Figs. 4c,d). For the large basin, the U velocity from the surface to ~600 m appears to be slightly greater for the weak-stability case, which may be explained by the stronger vertical momentum transfer associated with weaker stratification.

The heat-budget analysis, presented in Fig. 6, shows the various components of the potential temperature perturbation heat-budget equation, which were derived from the terms of Eq. (2) below:

$$\frac{\partial \theta'}{\partial t} = -\overline{\rho} w \frac{\partial \overline{\theta}}{\partial z} - \mathbf{u} \cdot \nabla \theta' + \overline{\rho} K_h (\nabla \theta) + S. \qquad (2)$$

(I) (II) (III) (IV) (V)

Term I represents the total potential temperature perturbation tendency or rate of change, term II represents the vertical advection of the base-state potential temperature tendency, term III is the vertical and horizontal advection tendencies, where $\mathbf{u}$ is the total wind vector, and term IV is the turbulent mixing tendency, where ρ and K_h are the density and thermal turbulent diffusivity of air, respectively. Term V represents the diabatic heating/cooling terms from microphysical processes and atmospheric radiative forcings or radiative flux divergence. Because microphysics was not accounted for in our simulations, term V represents solely the effect of cooling by radiative flux divergence. In our model, once the soil temperature is calculated by solving the surface energy-budget equation, thermal energy conservation of atmospheric layers is carried out. Heat is then transferred from the surface to upper-air layers by the potential temperature perturbation tendency described by Eq. (2). As shown in Fig. 6, the dominant cooling process inside the basin's cold-air pool is the radiative flux divergence, which is greater than the advective and turbulent mixing terms by an order of magnitude and is confined to near-surface locations (<200 m high), having its strongest cooling gradient for the first three grid points above the surface (<30 m). These results illustrate the physical process responsible for the temperature profiles

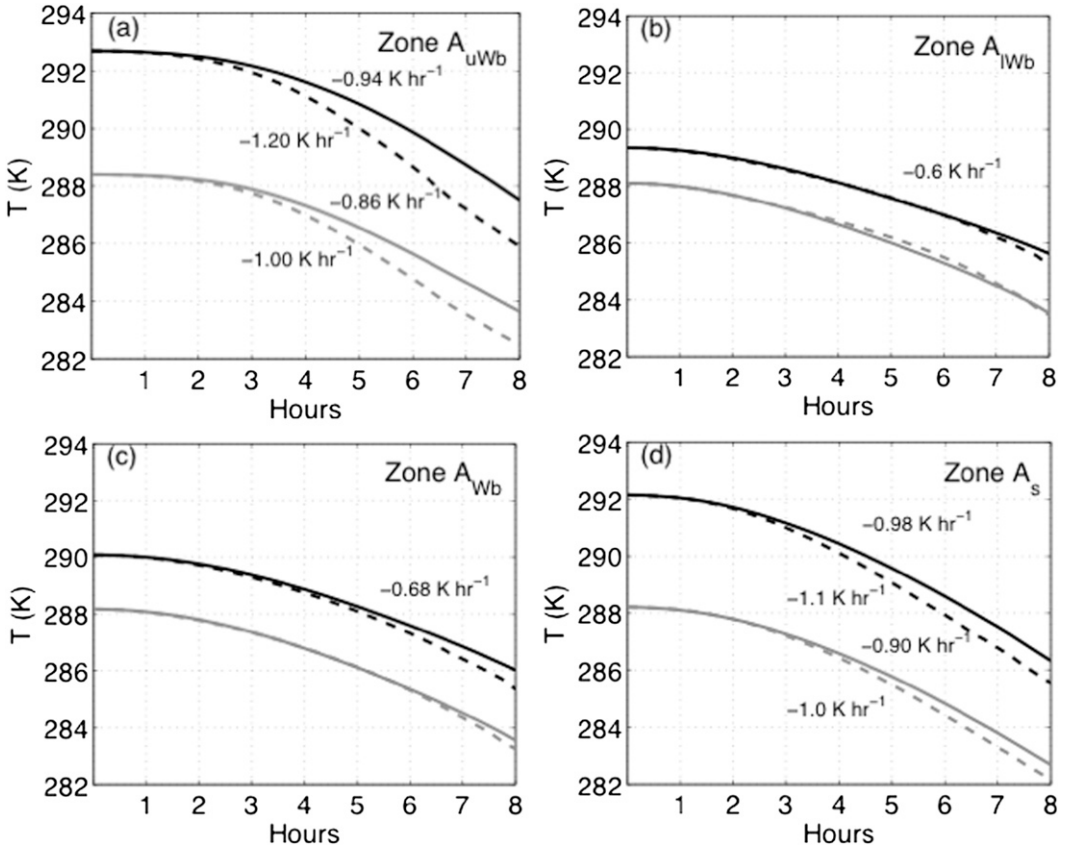

FIG. 7. Spatially averaged temperatures showing cooling rates for different basin zone areas (see Fig. 1a). Solid (dashed) lines represent the large (small) basin, and black (gray) lines represent the cases of strong (weak) stability. The large and small basins correspond to the upper-left and lower-right points in Fig. 1.

and its spatiotemporal evolution as discussed above and highlight the importance of longwave radiative flux divergence in the cooling process for near-surface air under very weak wind speed conditions.

c. *Basin cooling trends and minimum temperatures*

To illustrate the impact of basin size, slope angle, and stability on minimum temperatures and cooling trends within the basin environment, Figs. 7 and 8 show spatial and temporal averaging of temperatures within different cross-sectional areas (or zones) of the basin as defined in Fig. 1a. The cooling trends start to differ after ~3 h, and this is when the surface-layer inversion and the slope flows begin to develop in the simulations to an extent that influences the temperatures within the basin. The smallest basin cools at a faster rate than the largest basin for all of the zones within the basin (Fig. 7a). Observations of cooling trends in valleys and basins of different sizes (De Wekker and Whiteman 2006) also suggest this relation. The largest differences occur in the upper half of the basin (A_{uWb}) where the smallest basin size cools faster, while the cooling rate of the lower half of the basin (A_{lWb}) appears to be insensitive to the basin size and ambient stability and cools at a smaller rate (-0.6 K h^{-1}; Fig. 7b) relative to the upper half of the basin. The cooling rate over the slope area A_s was less sensitive to basin size and background stability (Fig. 7d). The weaker-stability case, in general, produces smaller cooling rates when compared with the strong-stability case.

The effect of the slope angle on the spatially averaged temperatures for the entire basin area A is highlighted in Fig. 8. In general, the entire 8-h average of basin temperature only varied by less than 2 K for the entire range of selected slope angles and basin sizes. The weaker-stability case (Fig. 8b) exhibits a larger temperature range, but still within the 2-K limits. For a fixed slope angle the mean basin temperature decreases with decreasing basin area, as shown by the solid lines connecting the points in Fig. 8. For both stability cases, increasing the slope angle leads to a warmer basin (see the dashed lines in Figs. 8a,b) despite the fact that the basin area also decreases. This could be explained by the fact that the greater the slope angle is, the weaker are the

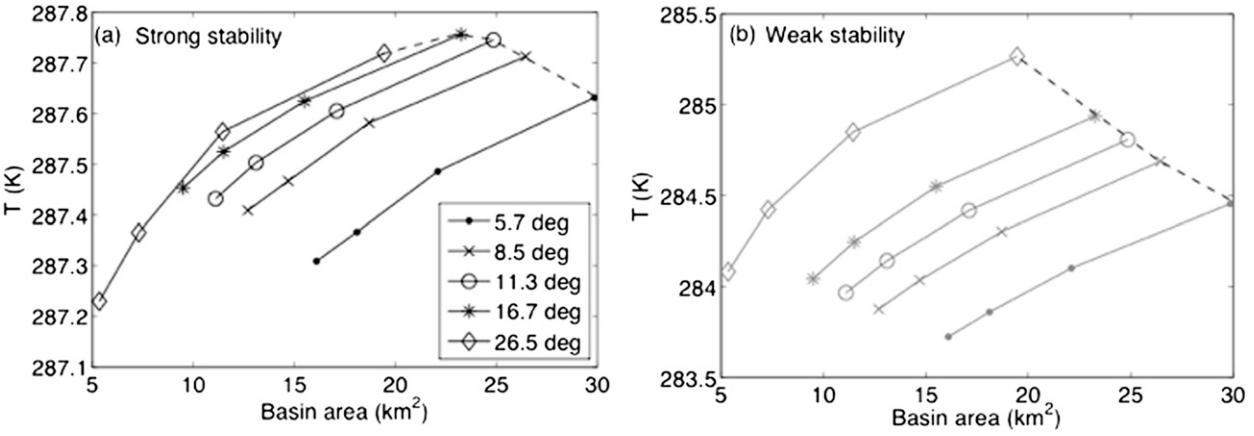

FIG. 8. Spatially averaged (over the entire area A of the basin; see Fig. 1a) temperature for the 8-h-averaged period as function of basin area, slope angle, and ambient stability.

slope winds (as discussed earlier), and thus there is weaker convergence in the basin center, which consequently leads to weaker vertical lifting and less adiabatic cooling. This effect is more pronounced for the weaker-stability case associated with a more neutral atmosphere.

4. Conclusions

A total of 40 two-dimensional fine-resolution numerical simulations using the ARPS model have been carried out to study the basic characteristics of a cold-air pool within basins of different sizes and slope angles and under different ambient stabilities. No complex phenomena such as low-level clouds or surface-type heterogeneity were included, but all other physical processes are accounted for in the simulations.

The main findings can be summarized as follows:

- The maximum downslope wind speed is strongly correlated with the basin size and slope angle, with stronger downslope winds corresponding to larger basin areas and lower slope angles. As basin area increases, the influence of slope angle on slope wind weakens and the maximum downslope wind is found farther down the slope.
- The cold-air pooling process appears to affect the downslope wind speed more strongly for smaller basins when more cold air is accumulated and the stable layer deepens as compared with larger basins.
- The smaller basin produces more cooling of the upper-basin layers with a vertical temperature structure that is closer to isothermal in the interior of the basin than is that in larger basins. The main physical process governing the cooling process near the basin floor (<200 m in height) was found to be longwave radiative flux divergence, whereas vertical advection of temperature dominated the cooling process for the upper-basin areas.
- As a result of the latter point, the mean cooling rates of the upper half of the basin are more sensitive to the basin size and ambient stability than are the lower half or the slope area. The lower half of the basin cooled at the slowest rate, as revealed from the deficit in temperature tendencies in that area from the heat-budget analysis, whereas the near-surface-layer cooling rate appears to be close to the upper-basin cooling rate at about 1 K h^{-1}.
- The relationships among the slope winds, basin area, and slope angle appear to be insensitive to atmospheric stability. The amount of cooling, especially in upper-basin layers, however, is affected by stability, with weaker stability allowing for more adiabatic cooling and thus a cooler basin in comparison with the stronger-stability case.

These results provide an insight into the cold-air pooling process and how the process is affected by topography and stability. Future work may include more factors such as snow cover, moisture exchanges, and low-level fog and stratus, as well as three-dimensional real case scenarios.

Acknowledgments. This research was supported by the U.S. National Science Foundation under Grants 0938401 and 0837860. Any opinions, findings, and conclusions or recommendations expressed in this material are those of the author(s) and do not necessarily reflect the views of the National Science Foundation. The simulations were performed partially on supercomputer BlueFern, managed and operated by the High Performance Computing Centre at the University of Canterbury, New Zealand, and partially on Bluefire,

managed and operated by the Computational and Information Systems Laboratory (CISL) at the U.S. National Center for Atmospheric Research. The authors thank Mike Kiefer, Xindi Bian, Jay Charney, Warren Heilman, Sebastian Hoch, John Horel, and Dave Whiteman for useful discussions. The authors also acknowledge the time and professional dedication that the anonymous reviewers put in to refine this research.

REFERENCES

Baines, P. G., 2001: Mixing in flows down gentle slopes into stratified environments. *J. Fluid Mech.,* **443,** 237–270.

Beare, R. J., and Coauthors, 2006: An intercomparison of large-eddy simulations of the stable boundary layer. *Bound.-Layer Meteor.,* **118,** 247–272.

Chou, M. D., 1990: Parameterization for the absorption of solar radiation by O_2 and CO_2 with application to climate studies. *J. Climate,* **3,** 209–217.

——, 1992: A solar radiation model for climate studies. *J. Atmos. Sci.,* **49,** 762–772.

——, and M. J. Suarez, 1994: An efficient thermal infrared radiation parameterization for use in general circulation models. NASA Tech. Memo. 104606, 85 pp. [Available from NASA Center for Aerospace Information, 800 Elkridge Landing Road, Linthicum Heights, MD 21090-2934.]

Chow, F. K., A. P. Weigel, R. L. Street, M. W. Rotach, and M. Xue, 2006: High-resolution large-eddy simulations of flow in a steep alpine valley. Part I: Methodology, verification, and sensitivity experiments. *J. Appl. Meteor. Climatol.,* **45,** 63–86.

Clements, C. B., C. D. Whiteman, and J. D. Horel, 2003: Cold-air-pool structure and evolution in a mountain basin: Peter Sinks, Utah. *J. Appl. Meteor.,* **42,** 752–768.

De Wekker, S. F. J., and C. D. Whiteman, 2006: On the time scale of nocturnal boundary layer cooling in valleys and basins and over plains. *J. Appl. Meteor. Climatol.,* **45,** 813–820.

Fedorovich, E., and Coauthors, 2004: Entrainment into sheared convective boundary layers as predicted by different large eddy simulation codes. Preprints, *16th Symp. on Boundary Layers and Turbulence,* Amer. Meteor. Soc., P4.7. [Available online at https://ams.confex.com/ams/pdfpapers/78656.pdf.]

Haiden, T., and C. D. Whiteman, 2005: Katabatic flow mechanisms on a low-angle slope. *J. Appl. Meteor.,* **44,** 113–126.

Hoggarth, A. M., H. D. Reeves, and Y. L. Lin, 2006: Formation and maintenance mechanisms of the stable layer over the Po Valley during MAP IOP-8. *Mon. Wea. Rev.,* **134,** 3336–3354.

Katurji, M., S. Zhong, and P. Zawar-Reza, 2011: Long-range transport of terrain-induced turbulence from high-resolution numerical simulations. *Atmos. Chem. Phys. Discuss.,* **11,** 9797–9829.

Klemp, J. B., and D. R. Durran, 1983: An upper boundary condition permitting internal gravity wave radiation in numerical mesoscale models. *Mon. Wea. Rev.,* **111,** 430–444.

Lee, T. J., R. A. Pielke, R. C. Kessler, and J. Weaver, 1989: Influence of cold pools downstream of mountain barriers on downslope winds and flushing. *Mon. Wea. Rev.,* **117,** 2041–2058.

Mahrt, L., 1982: Momentum balance of gravity flows. *J. Atmos. Sci.,* **39,** 2701–2711.

Malek, E., T. Davis, R. Martin, and P. Silva, 2006: Meteorological and environmental aspects of one of the worst national air pollution episodes (January, 2004) in Logan, Cache Valley, Utah, USA. *Atmos. Res.,* **79,** 108–122.

Monti, P., H. J. S. Fernando, M. Princevac, W. C. Chan, T. A. Kowalewski, and E. R. Pardyjak, 2002: Observations of flow and turbulence in the nocturnal boundary layer over a slope. *J. Atmos. Sci.,* **59,** 2513–2534.

Princevac, M., H. J. S. Fernando, and C. D. Whiteman, 2005: Turbulent entrainment into natural gravity-driven flows. *J. Fluid Mech.,* **533,** 259–268.

Rakovec, J., J. Merše, S. Jernej, and B. Paradiž, 2002: Turbulent dissipation of the cold-air pool in a basin: Comparison of observed and simulated development. *Meteor. Atmos. Phys.,* **79** (3-4), 195–213.

Reeves, H. D., and D. J. Stensrud, 2009: Synoptic-scale flow and valley cold pool evolution in the western United States. *Wea. Forecasting,* **24,** 1625–1643.

Smith, S. A., A. R. Brown, S. B. Vosper, P. A. Murkin, and A. T. Veal, 2010: Observations and simulations of cold air pooling in valleys. *Bound.-Layer Meteor.,* **134,** 85–108.

Steinacker, R., and Coauthors, 2007: A sinkhole field experiment in the eastern Alps. *Bull. Amer. Meteor. Soc.,* **88,** 701–716.

Weigel, A. P., F. K. Chow, M. W. Rotach, R. L. Street, and M. Xue, 2006: High-resolution large-eddy simulations of flow in a steep Alpine valley. Part II: Flow structure and heat budgets. *J. Appl. Meteor. Climatol.,* **45,** 87–107.

Whiteman, C. D., and S. Zhong, 2008: Downslope flows on a low-angle slope and their interactions with valley inversions. Part I: Observations. *J. Appl. Meteor. Climatol.,* **47,** 2023–2038.

——, X. Bian, and S. Zhong, 1999: Wintertime evolution of the temperature inversion in the Colorado plateau basin. *J. Appl. Meteor.,* **38,** 1103–1117.

——, S. Zhong, W. J. Shaw, J. M. Hubbe, X. Bian, and J. Mittelstadt, 2001: Cold pools in the Columbia Basin. *Wea. Forecasting,* **16,** 432–447.

——, T. Haiden, B. Pospichal, S. Eisenbach, and R. Steinacker, 2004: Minimum temperatures, diurnal temperature ranges, and temperature inversions in limestone sinkholes of different sizes and shapes. *J. Appl. Meteor. Climatol.,* **43,** 1224–1236.

Wolyn, P. G., and T. B. McKee, 1989: Deep stable layers in the intermountain western United States. *Mon. Wea. Rev.,* **117,** 461–472.

Xue, M., K. K. Droegemeier, and V. Wong, 2000: The Advanced Regional Prediction System (ARPS)—A multi-scale nonhydrostatic atmospheric simulation and prediction model. Part I: Model dynamics and verification. *Meteor. Atmos. Phys.,* **75** (3-4), 161–193.

——, and Coauthors, 2001: The Advanced Regional Prediction System (ARPS)—A multi-scale nonhydrostatic atmospheric simulation and prediction tool. Part II: Model physics and applications. *Meteor. Atmos. Phys.,* **76** (1-4), 143–165.

Yoshino, M. M., 1984: Thermal belt and cold air drainage on the mountain slope and cold air lake in the basin at quiet, clear night cold air drainage intermittent nature of the flow. *GeoJournal,* **8** (3), 235–250.

Zängl, G., 2005: Formation of extreme cold-air pools in elevated sinkholes: An idealized numerical process study. *Mon. Wea. Rev.,* **133,** 925–941.

Zhong, S., and C. D. Whiteman, 2008: Downslope flows on a low-angle slope and their interactions with valley inversions. Part II: Numerical modeling. *J. Appl. Meteor. Climatol.,* **47,** 2039–2057.

——, ——, X. Bian, W. J. Shaw, and J. M. Hubbe, 2001: Meteorological processes affecting the evolution of a wintertime cold air pool in the Columbia Basin. *Mon. Wea. Rev.,* **129,** 2600–2613.